




## Article

# Efficient, Compact Mid-Infrared Sources: A Systematic Study of Intracavity Difference-Frequency Generation

Saeed Salimian Rizi <sup>1,\*</sup>, Liam G. K. Flannigan <sup>1</sup>, Alex Chiasson <sup>1</sup>, Tyler Kashak <sup>1</sup>, Daniel Poitras <sup>2</sup>  
and Chang-Qing Xu <sup>1</sup>

<sup>1</sup> Department of Engineering Physics, McMaster University, Hamilton, ON L8S 4L8, Canada; flannilg@mcmaster.ca (L.G.K.F.); cqxu@mcmaster.ca (C.-Q.X.)

<sup>2</sup> Advanced Electronics and Photonics Research Center, National Research Council Canada, Ottawa, ON K1A 0R6, Canada; daniel.poitras@nrc-cnrc.gc.ca

\* Correspondence: salimias@mcmaster.ca

**Abstract:** This study presents a compact intracavity difference-frequency generation (DFG) source designed for mid-infrared (mid-IR) applications. By optimizing overlap between the pump and signal beams, we obtained a black-box efficiency ( $\eta_{BB}$ ) of 3.4%  $W^{-1}$  and a maximum DFG output power of 63 mW at a wavelength of 3437 nm for a 50 mm long periodically poled lithium niobate (PPLN) crystal. The mid-IR laser was systematically studied for various PPLN lengths (29 mm, 40 mm, and 50 mm), demonstrating extensive tunability across a range of mid-IR wavelengths. Stability assessments over short-term (2 min) and long-term (2 h) periods were also investigated, showing stability values of 0.91% and 1.08%, respectively. These advancements position our DFG laser as a promising candidate for potential applications in greenhouse gas detection and satellite communication, addressing the growing demand for reliable and efficient mid-IR sources.

**Keywords:** nonlinear optics; difference-frequency generation; mid-infrared laser; DPSS laser; overlap; black-box efficiency



Received: 16 November 2024

Revised: 9 December 2024

Accepted: 27 December 2024

Published: 30 December 2024

**Citation:** Salimian Rizi, S.; Flannigan, L.G.K.; Chiasson, A.; Kashak, T.; Poitras, D.; Xu, C.-Q. Efficient, Compact Mid-Infrared Sources: A Systematic Study of Intracavity Difference-Frequency Generation. *Photonics* **2025**, *12*, 25. <https://doi.org/10.3390/photonics12010025>

**Copyright:** © 2024 by the authors. Licensee MDPI, Basel, Switzerland. This article is an open access article distributed under the terms and conditions of the Creative Commons Attribution (CC BY) license (<https://creativecommons.org/licenses/by/4.0/>).

## 1. Introduction

There has been a surge in demand for compact and efficient mid-infrared (mid-IR) sources delivering several milliwatts to hundreds of milliwatts. These mid-IR lasers play vital roles in fields such as environmental monitoring for greenhouse gas (GHG) detection, free-space optical communication, medical diagnostics, and spectroscopy. Accurately detecting and analyzing chemical compounds in the mid-IR range is of particular interest for addressing pressing environmental challenges. Additionally, the reduced attenuation and scintillation experienced by mid-infrared wavelengths make these wavelengths an interesting option for terrestrial and long-distance satellite free-space optical communication [1–6].

Mid-IR laser technology has seen significant progress recently, particularly in developing intracavity difference-frequency generation (IC-DFG) systems that leverage the nonlinear, optical properties of materials for efficient mid-IR wavelength generation [7–9]. However, it can be difficult to fully optimize all aspects of the system that affect device efficiency. A critical aspect is the overlap efficiency, which requires both longitudinal and transverse alignment of interacting waves within the optical cavity to maximize the output power. Improving the overlap efficiency can substantially enhance the output power and stability when using focused Gaussian beams. In our results, we observe a strong correlation between focused Gaussian beam theory and experimental data regarding the overlap efficiency, highlighting its importance in system optimization. Parameters such

as the length and temperature dependence of the chosen nonlinear medium, which is periodically poled lithium niobate (PPLN) in this instance, also significantly affect IC-DFG system performance [9–13]. Addressing these challenges is vital for maximizing the overall efficiency and ensuring reliable DFG-based mid-IR lasers in practical applications.

A common approach to evaluating DFG frequency converters involves several efficiency metrics. The primary metric, DFG efficiency ( $\eta_{DFG}$ ), is expressed as follows:

$$\eta_{DFG} = \frac{P_{DFG}}{P_{pump}P_{signal}} \times 100\% \quad (1)$$

This efficiency, typically given in units of  $\%W^{-1}$ , is calculated using the output DFG power,  $P_{DFG}$ , measured after the Ge filter, relative to the input pump power,  $P_{pump}$ , measured before the gain medium (in this case, before entering the Nd:YVO<sub>4</sub>), and the input signal power,  $P_{signal}$ , measured at the input facet of the nonlinear medium [14]. While this metric provides a general efficiency measure, it does not account for coupling losses or the efficiencies of the pump and signal sources themselves, which can be crucial in power-limited scenarios, where maximizing the output power for a given input power is essential.

To address this practical limitation, we include black-box efficiency ( $\eta_{BB}$ ), shown as follows:

$$\eta_{BB} = \frac{\eta_{pump}\eta_{signal}P_{DFG}}{P_{pump}P_{signal}} \times 100\% \quad (2)$$

where  $\eta_{pump}$  is the optical-to-optical efficiency of the fiber pump source, and  $\eta_{signal}$  is the efficiency of the fiber signal source. For setups using fiber lasers, such as 1064 nm Yb-doped fiber lasers (pumped by 980 nm diodes), typical efficiencies are around 60%, so we assume  $\eta_{pump} = 0.6$  [15]. For direct diode-pumped systems, we set  $\eta_{pump} = 1$  due to the lack of an additional optical conversion step. We also assume  $\eta_{signal} = 1$  for erbium-doped fiber amplifiers (EDFAs), which are commonly used in DFG setups. Although some EDFAs can achieve up to 80% efficiency [16], we omit this factor for simplicity, as all setups use EDFA-based signal lasers, meaning that this would equally lower the efficiency for all laser sources.

The third metric, internal efficiency ( $\eta_{internal}$ ), provides insight into how well the system converts signal power specifically. It is defined as:

$$\eta_{internal} = \frac{P_{DFG}}{P_{signal}} \times 100\% \quad (3)$$

This internal efficiency is useful for characterizing the system's conversion performance, independent of pump power contributions [17]. By examining these three metrics—DFG efficiency, black-box efficiency, and internal efficiency—we obtain a comprehensive understanding of the system's performance, facilitating a fair comparison across DFG structures.

In terms of efficiency metrics, our current work shows a notable advancement over previous studies. Compared to our previous paper (2023) [14], which reported both black-box efficiency ( $\eta_{BB}$ ) and DFG efficiency at 2.2% and an internal efficiency of 12.5%, our new setup demonstrates substantial gains. Specifically, we achieved an  $\eta_{BB}$  and  $\eta_{DFG}$  of 3.3% and an  $\eta_{internal}$  of 18.8%. This reflects a ~50% improvement in overall system effectiveness.

Guha's study, a representative example of the state of the art for high-power, single-pass mid-infrared generation, reported a  $\eta_{BB}$  of 0.159%  $W^{-1}$ ,  $\eta_{DFG}$  of 0.264%, and  $\eta_{internal}$  of 11.5% [18]. While their work emphasizes multi-watt power levels, our current  $\eta_{BB}$  is over twenty times higher, showcasing the significantly optimized efficiency of our intracavity system, even when accounting for both pump and signal source factors.

Similarly, Huang's 2019 work achieved a  $\eta_{BB}$  of 2.43%  $W^{-1}$  and a  $\eta_{DFG}$  of 6%, but with a lower  $\eta_{internal}$  at 6% [19]. While Huang's DFG efficiency remains relatively high, our work surpasses this with both a higher internal efficiency and a comparable BB efficiency.

Lastly, Junqing Zhao’s 2024 study reports a record  $\eta_{internal}$  of 33.3% [20]. Zhao emphasizes that their highest conversion efficiency is observed at a specific threshold pump power and claims that their result represents the highest average power produced from any single-pass parametric conversion source with  $>3 \mu\text{m}$  idler wavelength fed by a continuous-wave (CW) signal. However, Zhao’s  $\eta_{BB}$  is lower at 0.8%, and since this result was achieved under pulsed conditions, our results for continuous-wave operation signify a major advancement, demonstrating efficient power conversion without the gain enhancement seen in pulsed operation [20,21].

In summary, our new setup demonstrates a respectable performance across all three metrics, making it highly competitive and efficient for DFG applications. This design shows potential for practical applications in GHG detection and free-space optical communication, addressing the increasing demands for compact size, low power consumption, wavelength tunability, and high efficiency. By systematically optimizing the overlap efficiency and other critical parameters, we demonstrate the potential of this design to excel in these applications. This work not only advances the existing body of knowledge in mid-IR generation but also opens new avenues for applications in environmental sensing and telecommunications [22,23].

## 2. Method and Theory

### 2.1. Overview of Experimental Setup

The primary method used in this study is difference-frequency generation (DFG), a nonlinear, optical process in which two laser beams (a pump and a signal) interact within a nonlinear medium to generate an idler wave at a frequency equal to the difference between the pump and signal frequencies. DFG is particularly effective for generating mid-infrared (mid-IR) light, as it can convert the 1064 nm pump and a C-band signal (typically 1530–1565 nm) into an idler at approximately 3.5  $\mu\text{m}$ . This work leverages the availability of high-power, high-efficiency 1064 nm solid-state lasers and C-band fiber lasers combined with nonlinear materials like periodically poled lithium niobate (PPLN) to efficiently generate mid-IR radiation. The efficiency of DFG is influenced by several factors, including phase-matching conditions, beam intensities, and the properties of the nonlinear medium.

For a clear overview of the experimental setup, Figure 1 illustrates the layout of key components involved in the experiment, including the pump and signal sources, nonlinear medium, and output coupler. The figure provides a high-level summary of the components before delving into the specific details of each element.

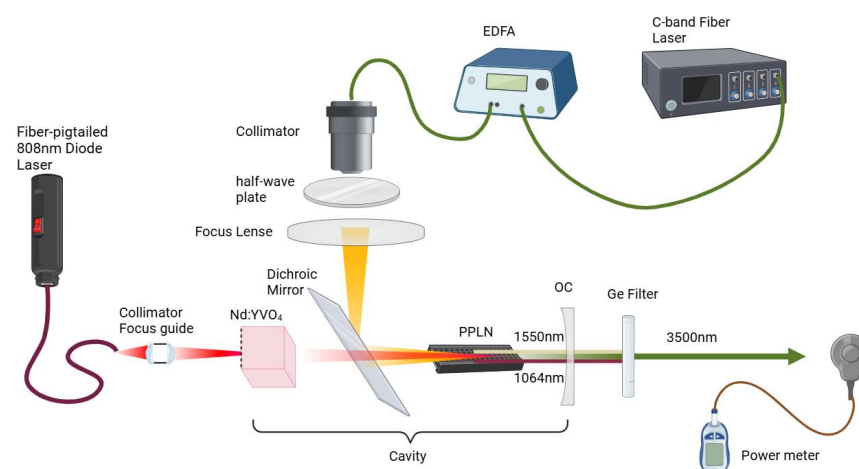


**Figure 1.** Experimental schematic diagram of the DFG setup. The 808 nm diode laser is coupled to the Nd gain medium, which is followed by a dichroic mirror and a PPLN crystal for frequency conversion. The optical layout includes a collimator, half-wave plate, and a plano-convex lens for focusing.

## 2.2. Experimental Components

Our experimental setup includes several key components, as outlined below:

- **Pump source:** A multimode fiber-pigtailed diode laser (AeroDIODE 808LD-2-0-0), emitting at 808 nm with up to 5 W of optical power, was used to pump the Nd:YVO<sub>4</sub> gain medium. The laser's output was focused onto the Nd medium through a collimator focus module (Edmund Optics #88–181 & 88–186), which ensures efficient coupling.
- **Gain medium:** The Nd:YVO<sub>4</sub> gain medium has an input facet that is high-reflection (HR) coated at 1064 nm (reflectivity > 99.9%) and high-transmission (HT) coated at 808 nm (transmission > 95%). The output facet is anti-reflection (AR) coated for 1064 nm (transmission > 99.8%).
- **Dichroic mirror:** A custom-fabricated dichroic mirror, made by the National Research Council, is used to transmit 99.3% of 1064 nm light and reflect 70% of 1541 nm light, ensuring effective coupling of the pump and signal beams into the nonlinear medium.
- **PPLN crystals:** Three MgO-doped PPLN crystals, each with a 5 mol.% MgO doping concentration and fabricated in-house, were used for DFG. The crystals had lengths of 29 mm, 40 mm, and 50 mm and a periodicity of 30.51 μm. The crystals were 1 mm thick and had poling duty cycles of 50%. These crystals were mounted to a copper heat sink with a thermoelectric cooler (TEC) that provided precise temperature control with an accuracy of 0.05 °C. The input facets of the PPLN crystals were AR coated for both 1064 nm and 1541 nm (transmission > 99.7%), while the output facets were AR coated for 1064 nm and approximately 3.5 μm (transmission > 95%).
- **Output coupler:** A custom-made CaF<sub>2</sub> plano-concave mirror with a 100 mm radius of curvature was used as the output coupler. It was HR coated for 1064 nm (reflectivity = 99.85%) and AR coated for ~3.5 μm (transmission = 92%).
- **Beam monitoring:** The DFG power was measured using a thermal power sensor (Thorlabs S401C) after the pump and signal beams were filtered out using a germanium (Ge) filter (Thorlabs WH91050-C9).

Additionally, a tunable C-band laser (Agilent 8164B) around 1541 nm was amplified through a polarization-maintained EDFA (CiviLaser EDFA-C-BA-26-PM). The output was collimated with a Thorlabs F110APC-1550 collimator, and a 100 mm focal length plano-convex lens (Thorlabs LA1050-C) focused the beam into the center of the PPLN. A half-wave plate (Thorlabs WPHSM05-1550) was inserted between the focusing lens and collimator to adjust polarization. This arrangement was simulated in Zemax, predicting an ~80 μm beam waist radius at the PPLN center.

## 2.3. DFG Power Estimation

To estimate the expected DFG output power, we began by simulating the cavity using spatially dependent rate equations to calculate the circulating intracavity power, followed by applying nonlinear wave equations for DFG to predict the output power, initially disregarding beam overlap effects [14]. This approach allowed us to assess the impact of nonlinear conversion, which introduces additional pump loss within the cavity dubbed the nonlinear loss. After deriving an initial estimate for DFG power, we calculated a nonlinear loss factor and reran the intracavity simulation. This iterative process continued until both power levels converged to a stable value, where stable is defined as a negligible change in the magnitude of the power between iterations. Ultimately, the nonlinear loss in this experiment was negligible, as the pump intensity far exceeded both the signal and DFG intensities by orders of magnitude. However, as the signal and DFG intensities approach the pump's in magnitude, nonlinear losses from depletion would become significant.

The cavity simulation builds on our prior research on intracavity DFG sources, utilizing a spatially dependent rate equation model taking into account the transverse wave distribution inspired by Risk’s methodology [24]. This model facilitates the estimation of the intracavity 1064 nm pump power. With the input pump and signal powers established, the nonlinear wave equations governing DFG are applied to estimate the output idler power, as described in Equations (4) and (5) [25]:

$$\frac{dA_1}{dz} = \frac{2id_{eff}\omega_1^2}{k_1c^2} A_3A_2^*e^{i\Delta kz} \tag{4}$$

$$\frac{dA_2}{dz} = \frac{2id_{eff}\omega_2^2}{k_2c^2} A_3A_1^*e^{i\Delta kz} \tag{5}$$

In these equations, A1 denotes the amplitude of the signal wave, A2 the amplitude of the idler wave, and A3 the amplitude of the pump wave. This approach assumes a constant cavity pump power, as the DFG conversion efficiency is low enough in this configuration to render nonlinear conversion losses negligible. This assumption remained valid even at the highest pump powers, as the DFG conversion efficiency was not large enough to significantly deplete the 1064 nm power.

We varied the PPLN’s operating temperature using the TEC to achieve optimal output power, thereby enabling phase matching across different temperatures for varying PPLN lengths and signal wavelengths. The PPLN’s temperature response was modeled with the MgO-doped Sellmeier equation [26]. Through this model, we reliably predict both the DFG output power as a function of input pump power and the DFG power’s temperature dependence via the Sellmeier equation. These predictions, presented alongside experimental results in the Results section, show strong alignment. Table 1 details the simulation parameters, distinguishing values measured or simulated in this study as “This work,” while cited values reference the existing literature.

**Table 1.** Simulation input parameters for the DFG model, with experimentally determined or simulated values noted as “This work” and referenced values sourced from the literature.

Parameter	Value	Ref.
Nonlinear coefficient ( $d_{33}$ )	27 pm/V	[14]
Nd: YVO <sub>4</sub> length (l)	8 mm	This work
Output coupler transmission (T) at 1064 nm	0.15%	This work
Round-trip losses (L)	3%	This work
Absorption efficiency $\eta_a$	99%	This work
Boltzmann factor (f)	0.6	[14]
Upper manifold lifetime ( $\tau$ )	90 $\mu$ s	[14]
1064 nm lasing beam radius ( $\omega_L$ ) at the output coupler	190 $\mu$ m	This work
808 nm pump beam radius ( $\omega_P$ )	225 $\mu$ m	This work
1064 nm pump beam radius in PPLN	100 $\mu$ m	This work
Signal beam radius in PPLN	80 $\mu$ m	This work
Nd doping	0.5 at. %	This work
PPLN refractive index	$\sim$ 2.2	[14]
Stimulated emission cross-section ( $\sigma$ )	$25 \times 10^{-19}$ cm <sup>2</sup>	[14]

#### 2.4. Overlap Efficiency

The overlap efficiency of the DFG process is also a critical factor in optimizing DFG processes, determining how effectively the interacting pump and signal beams combine within the nonlinear medium. Higher overlap efficiency translates to improved energy conversion and higher output power. Following the methodologies outlined by Guha and Falk [13,18], we employed overlap integrals to quantify system efficiency, emphasizing



the importance of engineering beam diameters to enhance overlap efficiency. While their paper outlines a single-pass approach, we have found, using the previously described cavity simulation to estimate the circulating 1064 nm pump power and using ABCD matrix resonator modeling software (reZonator version. 2.0.13-beta9) to estimate the pump and signal beam sizes in the PPLN, that the simulation results are a good match for our intracavity device as well [27]. By carefully adjusting the beam sizes and geometries, we can significantly improve the overall DFG efficiency.

The general idea is to integrate over the entire plane of the output crystal facet to obtain the output idler power for a given pump and signal power. The result of the derivation is the complex double integral  $h$  with many variable terms, found below [13,18,28]:

$$h = \left(\frac{1}{4\zeta_4}\right)II = \int_0^l \int_0^l dz_1 dz_2 \times \frac{\exp[i\Delta kl(z_1 - z_2)]\exp\left[-\left(\frac{4B^2}{\alpha}\right)(z_1 - z_2)^2 f\right]}{(z_1 - A)(z_2 - A_1^*) + C_1} \tag{6}$$

where

$$\begin{aligned} k &= \frac{k_1}{k_2} \\ B &= \frac{\rho}{2} \left(\frac{l(k_1+k_2)}{2}\right)^{\frac{1}{2}} \\ \zeta_1 &= l/(2z_{R1}) \\ \zeta_2 &= l/(2z_{R2}) \\ \zeta_3 &= \frac{\zeta_1\zeta_2(1+k)}{\zeta_2+k\zeta_1} \\ \zeta_4 &= \frac{\zeta_1+k\zeta_2}{1+k} \\ \alpha &= \frac{\zeta_1+k\zeta_2}{(1+k)\zeta_1\zeta_2} \\ A_1 &= \frac{1}{2} + \frac{i}{4} \left(\frac{1}{\zeta_3} + \frac{1}{\zeta_4}\right) \\ C_1 &= -\frac{1}{16} \left(\frac{1}{\zeta_3} - \frac{1}{\zeta_4}\right)^2 \\ z'_3 &= \frac{1}{2} + \frac{i}{2\zeta_3} \end{aligned} \tag{7}$$

and

$$f = \frac{(z_1 - z'_3)(z_2 - z'_3^*)}{(z_1 - A_1)(z_2 - A_1^*) + C_1} \tag{8}$$

$z_1$  and  $z_2$  are the positions of the waves inside of the nonlinear medium along the optical axis of propagation. The integral result,  $h((\Delta kl), \zeta_1, \zeta_2, k, B)$ , incorporates several variables:  $\Delta kl$  (phase mismatch across crystal length  $l$ ), the focus factors  $\zeta_i$ , calculated by dividing the crystal length by twice the Rayleigh range of each beam, and  $k$ , the pump-to-idler wavenumber ratio. For our setup with PPLN, the phase walk-off term  $B$  is zero. By tuning the phase mismatch through PPLN temperature adjustments, we maximized  $h$  for each crystal. Once optimized,  $h$  is mainly dependent on the focus factors, allowing us to analyze the effect of the beam size on the output power, which is presented in the Results section. The simulation outputs are then directly compared to experimental data in the subsequent section.

### 3. Results

#### 3.1. DFG Power and Black-Box Efficiency

Figures 2 and 3 display the DFG mid-infrared (mid-IR) output power and black-box efficiency relative to 808 nm pump power across different lengths of periodically poled lithium niobate (PPLN). Insets in these figures identify each PPLN length, enabling a direct comparison of length-dependent DFG performances. Specifically, the red circle represents the 50 mm PPLN, the green square corresponds to the 40 mm PPLN, and the purple triangle denotes the 29 mm PPLN. The x-axis indicates the 808 nm pump power, while the y-axis shows the DFG power output measured post-Ge filter.

Upon coupling the EDFA signal into the 50 mm PPLN, we obtained DFG power levels up to 63 mW at 3437 nm, with an 808 nm pump power of 4.7 W and a signal power of 400 mW (measured at the output of the focusing lens). This setup yielded a black-box efficiency of  $3.4\% \text{ W}^{-1}$ . Experimental data points are represented by shapes, while the solid line shows simulated DFG power based on the assumption that both input beams are focused at the PPLN center. The cavity loss was treated as a fitting variable, with all other input variables experimentally measured.

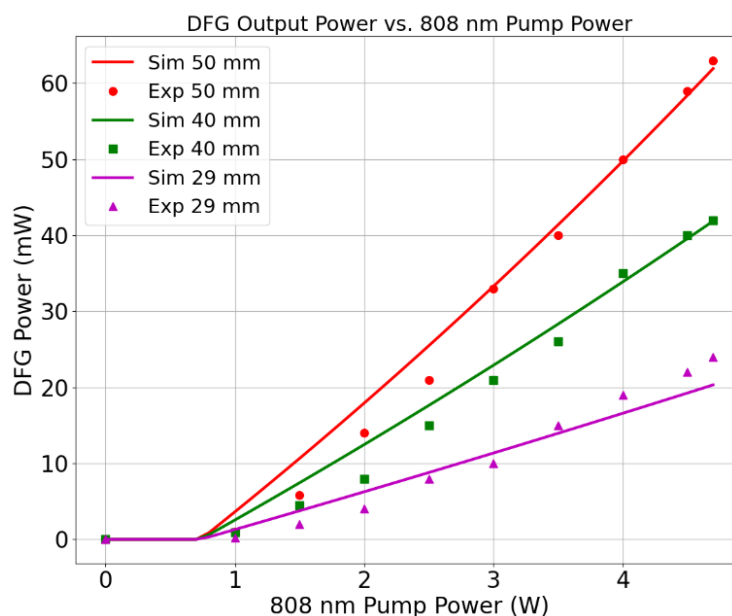


**Figure 2.** Measured and simulated DFG mid-infrared output power as a function of 808 nm pump power for three different periodically poled lithium niobate (PPLN) lengths: 29 mm (purple triangles), 40 mm (green squares), and 50 mm (red circles). The x-axis represents the pump power, while the y-axis shows the DFG output power after the germanium (Ge) filter. The solid lines represent simulated DFG power, assuming both input beams are focused at the PPLN center. The inset shows the three PPLN lengths tested, highlighting their significant impact on DFG performance characteristics. The DFG threshold remains nearly constant for different PPLN lengths because it is primarily determined by the intracavity 1064 nm laser, which is influenced by cavity losses. These losses have negligible dependence on PPLN length, since the propagation loss within the PPLN is insignificant.

The results reveal that an increase in the crystal length leads to higher DFG output power and black-box efficiency, which is expected due to the extended nonlinear interaction length. Data collection was conducted at a fixed temperature and signal power while varying the pump power. The close alignment between the simulation results and experimental data underscores the robust performance of the system, with these measurements representing the highest recorded black-box efficiency. There is a dip in the experimental efficiency versus the simulated efficiency for the longer crystal, which could be explained by small differences in the simulation assumptions versus the experimental conditions. The efficiency for focused Gaussian beams is highly dependent on both the beam sizes as well as beam positions in the crystal, and the phase-matching condition is more difficult to maintain over larger crystals. As a result, this small discrepancy could be explained by differences in the beam positions, small changes in the beam radii, and difficulty in maintaining a constant temperature of the longer PPLN for focused Gaussian beams, all of which could add up to a noticeable difference between the simulation and experiment. It would be possible to spend more time fitting variables to the experimental data to achieve a tighter fit, but the overall agreement in the trend was good enough that this was deemed unnecessary.

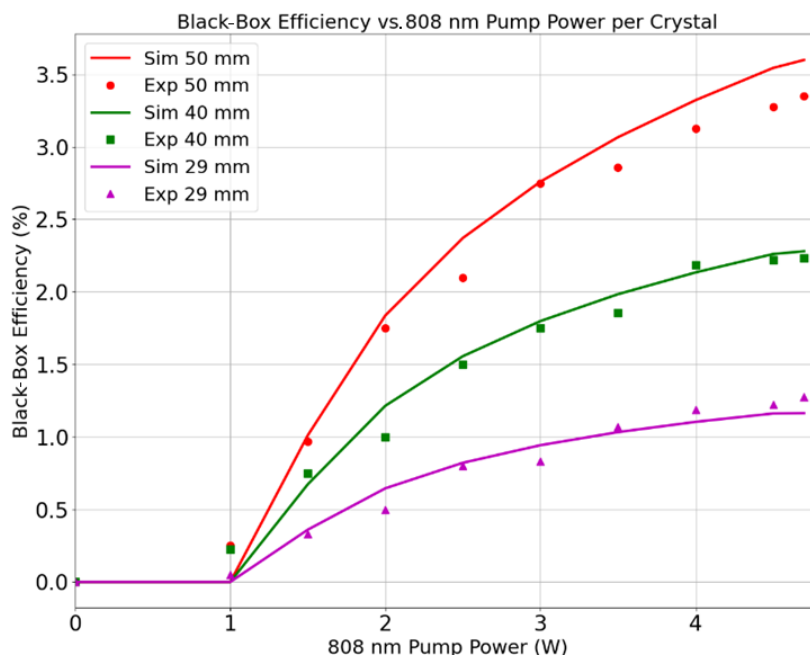


**Figure 3.** Measured and simulated DFG black-box efficiency versus 808 nm pump power for the same PPLN lengths: 29 mm (purple triangles), 40 mm (green squares), and 50 mm (red circles). The solid lines represent the simulated DFG black-box efficiency, while the markers indicate the experimental data. Data were obtained under constant temperature conditions, with significant findings demonstrating that longer PPLN lengths result in enhanced DFG power and black-box efficiency. The inset illustrates the three PPLN lengths tested, emphasizing their role in influencing DFG performance metrics.

This dataset highlights the efficiency of our system, demonstrating the ability to achieve substantial output power while ensuring effective phase matching. Overall, the findings are promising, not only showing strong agreement with theoretical predictions but also suggesting that overlap efficiency optimization can further enhance the output power, which is relevant for applications like greenhouse gas detection and optical communication [6].

### 3.2. Beam Overlap Characterization

In this section, we analyze the beam overlap between the pump and signal beams within the nonlinear crystal, aiming to identify potential efficiency improvements. Based on Equation (7), the pump focus factor,  $\zeta_p$ , is held constant at 0.394, corresponding to a 100  $\mu\text{m}$  beam radius from the cavity simulation for the pump at 1064 nm. We plot the overlap integral  $h$  versus the signal focus factor  $\zeta_s$ , as shown in Figure 4. The simulated overlap integral  $h$  reaches higher values at lower  $\zeta_s$  values, with an optimized focus lens achieving a simulated  $h$  value of 0.09282 at a  $\zeta_s$  value of 0.8922. Experimentally, the red triangle indicates the previous setup [14] using an F280 collimator, where  $h = 0.0652$  at  $\zeta_s = 3.23$ , reflecting the limitations of the prior configuration. The red square represents the new setup with an optimized F110 lens, achieving an  $h$  value of 0.09282 at  $\zeta_s = 0.8922$ , a value close to the simulation but slightly lower due to minor alignment and modeling discrepancies in thermal lensing for the pump beam.



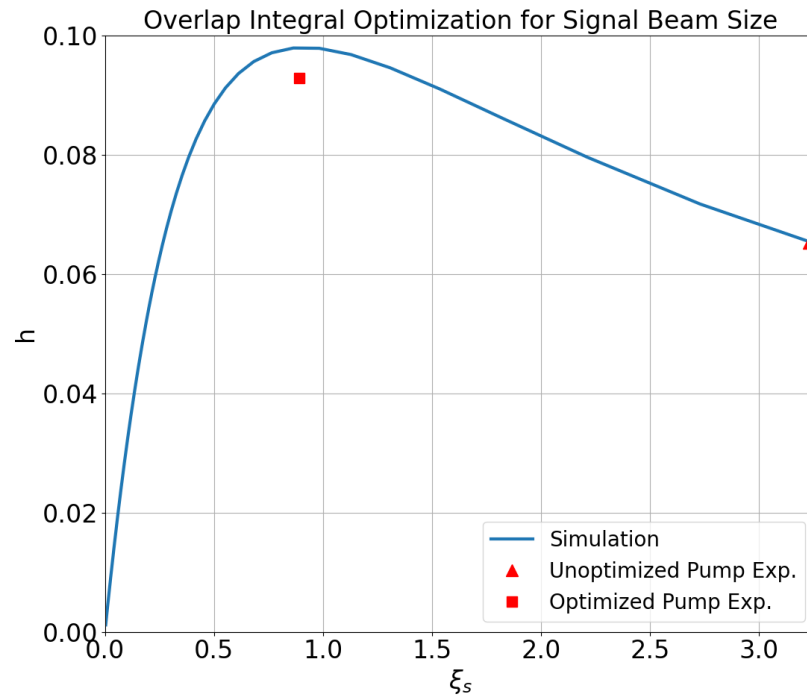


**Figure 4.** A plot of the overlap integral for the current device, represented by the blue curve. The square dot indicates the optimized overlap efficiency for the current device, while the triangular dot represents the non-optimized overlap from previous work [14]. This comparison highlights the improvements in overlap efficiency achieved with the current design. The horizontal axis represents the signal focus factors ( $\xi_s$ ), calculated by dividing the crystal length by twice the Rayleigh range of the signal beam. The vertical axis represents the overlap integral ( $h$ ), which is discussed in detail in Section 2.4 of the manuscript.

To quantify the expected efficiency gain, we calculate an overall theoretical efficiency boost based on the ratio of overlap integrals and input powers:

$$(h_{new}/h_{old}) \times (400\text{ mW}/330\text{ mW})_{1541\text{nm power}} \times (4.7/4.5\text{ W})_{808\text{nm pump power}}$$

This theoretical boost results in an estimated 88% increase, while the experimental value reaches 80%, aligning closely with the simulated expectations. This 80% efficiency increase, derived as 63 mW/35 mW, verifies the effectiveness of the optimized configuration.

Focusing the pump beam more tightly to improve overlap even further in the current setup presents challenges due to the hemispherical cavity design. The pump beam size is limited by the strength of the thermal lens, with stronger thermal lenses leading to theoretically smaller pump beam radii, which would improve the efficiency up to the theoretical maximum at a pump and signal focus factor approaching 2.2–2.8. However, at a certain point, we will reach the limit of cavity stability, limiting how much we can further focus the pump beam over the current radius. The hemispherical cavity was selected to keep the design compact, but to truly optimize the pump beam overlap as well as the signal beam overlap, a new cavity design is likely needed. Nonetheless, the current cavity design provides a reasonable efficiency that agrees well with theory, and the compact form factor provided by the hemispherical cavity means the device is useful for keeping the device’s weight and volume down. A previous study from our group on a similar SFG-based design showed that by optimizing the pump and signal beam fully, the efficiency increase over the previous design could be >90%, so it is worth pursuing in future work [28].

### 3.3. Wavelength Tunability and Temperature Tolerance of the DFG Laser

To evaluate the temperature tolerance and tunability of the DFG laser, we examined the temperature tuning curve of the DFG power across three different PPLN lengths. This study involved both experimental measurements and simulations using the Sellmeier equation for MgO-doped lithium niobate [26]. Figure 5 shows the normalized DFG power as a function of the PPLN temperature, with the experimental data indicated by squares for the 40 mm PPLN, triangles for the 29 mm PPLN, and circles for the 50 mm PPLN, while the simulation results are depicted by a solid line. The close alignment between the experimental and simulated peak power locations, as well as the Full Width at Half Maximum (FWHM), validates the accuracy of our model and confirms DFG output generation. The actual values of the FWHM in degrees Celsius are as follows: 7 degrees (50 mm), 8.25 degrees (40 mm), and 10.7 degrees (29 mm).

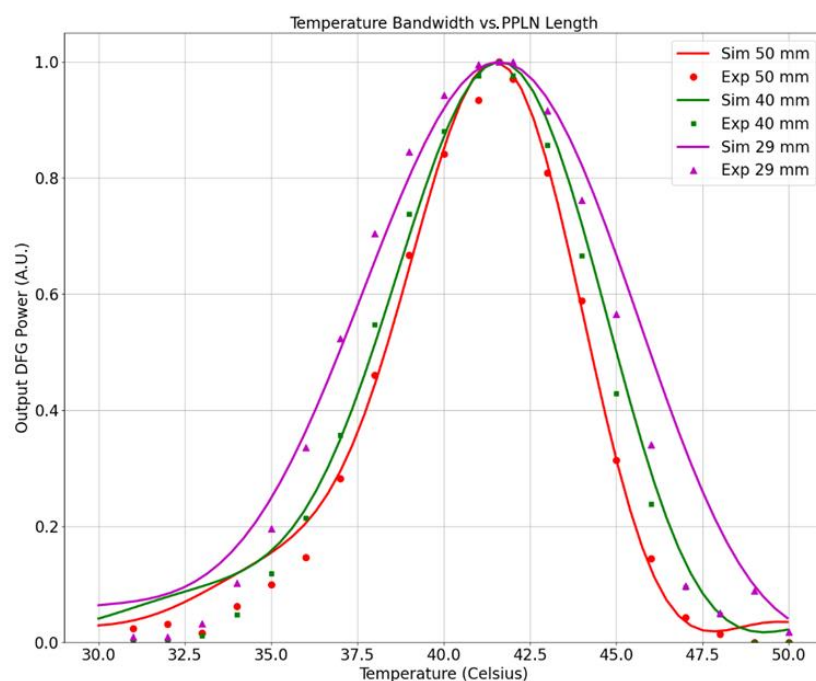


**Figure 5.** The temperature tuning curve of DFG power as a function of the PPLN temperature for three lengths—29 mm, 40 mm, and 50 mm—with corresponding constant signal wavelengths of approximately 1541 nm. The close matching between the experimental data (triangles for 29 mm, squares for 40 mm, and circles for 50 mm) and the simulated results (solid line) validates the accuracy of the model. The Full Width at Half Maximum (FWHM) values are approximately 10.7 °C (29 mm), 8.25 °C (40 mm), and 7 °C (50 mm), confirming stable DFG output.

In nonlinear optics phenomena, this change in the FWHM can be derived from phase-matching considerations and is often expressed using a  $\text{sinc}^2$  function. For a nonlinear process to achieve efficient phase matching, the interaction must maintain coherence over the entire length of the PPLN crystal. However, the phase-matching bandwidth becomes narrower as the crystal length increases. This effect arises because longer crystals impose stricter requirements for phase matching due to the  $\text{sinc}^2$  function, and the temperature tuning the FWHM is inversely related to the crystal length [8,29].

Our results demonstrate that as the PPLN length increases, the tunability decreases; specifically, the 50 mm crystal exhibited slightly lower tunability compared to the shorter crystals, yet it achieved higher output power. This is the expected behavior from theory, so confirming this experimentally serves as a useful check that we are observing DFG governed by focused Gaussian beam theory.

The stability of the measurements was achieved using a standard thermoelectric cooler paired with an in-house machined copper heat sink, which also served as the crystal housing. Overall, the experimental data matches well with the simulation results, confirming the reliability of our modeling approach and the effectiveness of the DFG system.

For wavelength tunability, the DFG laser output was further characterized by fixing the PPLN temperature at two-degree intervals from 16 °C to 56 °C, where the thermoelectric cooler (TEC) functions optimally, and adjusting the multiwavelength C-band fiber laser. The C-band fiber laser provides signal light from 1530 nm to 1555 nm with 1 nm spacing steps, a total power of nearly 380 mW, and a bandwidth of approximately 0.085 nm (FWHM) at 1540 nm. The pump bandwidth at 1064 nm is around 0.5 nm. Figure 6 presents the simulated DFG output power for the 40 mm PPLN, yielding a peak power of around 42 mW, as previously reported, with a signal bandwidth of 1539–1552 nm (approximately 13 nm). This corresponds to an idler tunability of ~3390–3440 nm or 50 nm, which is illustrated on the secondary x-axis at the top of Figure 6.

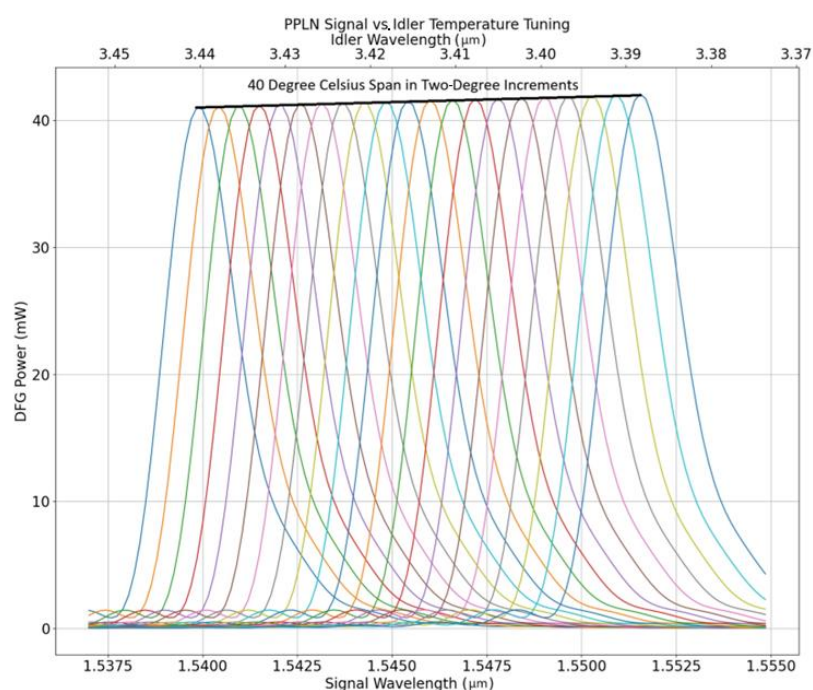


**Figure 6.** Simulated DFG output power as a function of the signal wavelength for a 40 mm PPLN at varying temperatures. The graph demonstrates the broad wavelength tunability of the DFG laser source, with a peak power of approximately 42 mW across a signal bandwidth of 1539 to 1552 nm.

In the experiment, a temperature change of 40 °C resulted in a tuning bandwidth of 12 nm, while the simulation indicated a bandwidth of about 13 nm for a temperature change of 48 °C, showing good agreement with the experimental data. These results highlight the broad wavelength tunability of our DFG laser source, which is critical for applications requiring precise mid-IR control. Using the Full Width at Half Maximum of the curve for the leftmost peak in Figure 6 corresponding to a temperature of 16 °C and a peak signal wavelength of ~1540 nm, the idler output bandwidth spans 3447–3457 nm or ~10 nm. These results highlight the broad wavelength tunability of our DFG laser source, which is critical for applications requiring precise mid-IR control.

As previously discussed in Figure 5, while variations in the PPLN length influence the Full Width at Half Maximum (FWHM) of the DFG output, they do not alter the center wavelength of the peak. This indicates that changes in the PPLN length affect the temperature tuning sensitivity rather than extending the wavelength range or tunability. Therefore, the

position of the peak remains almost constant across different PPLN lengths, demonstrating that length adjustments alone do not enhance tunability in terms of wavelength range. Instead, the PPLN length primarily impacts the FWHM, which can be optimized depending on the requirements for stability or sensitivity in specific applications.

Overall, these findings reinforce the importance of optimizing both the temperature and PPLN length to achieve the desired mid-IR wavelengths, underscoring our design's capability for applications in greenhouse gas (GHG) detection and free-space optical communication.

### 3.4. Stability Analysis

Stability over time is a crucial metric for assessing the reliability of an optical instrument. To evaluate this, the 1064 nm and EDFA modules were maintained at constant power, while the DFG output was monitored for two periods: a short-term duration of 2 min and a long-term duration of 2 h, with no adjustments made during measurement. DFG power was sampled every 2 s during the 2 min interval and every 5 s over the 2 h interval to ensure manageable data density. The resulting data, shown in Figure 7, were analyzed for stability, which was calculated as the root mean square deviation of the DFG dataset. Nonlinear DPSS-based lasers typically demonstrate stability values below 4% [30]. Our DFG setup exhibited a stability of 0.91% after 2 min and 1.08% after 2 h, aligning well within this range.

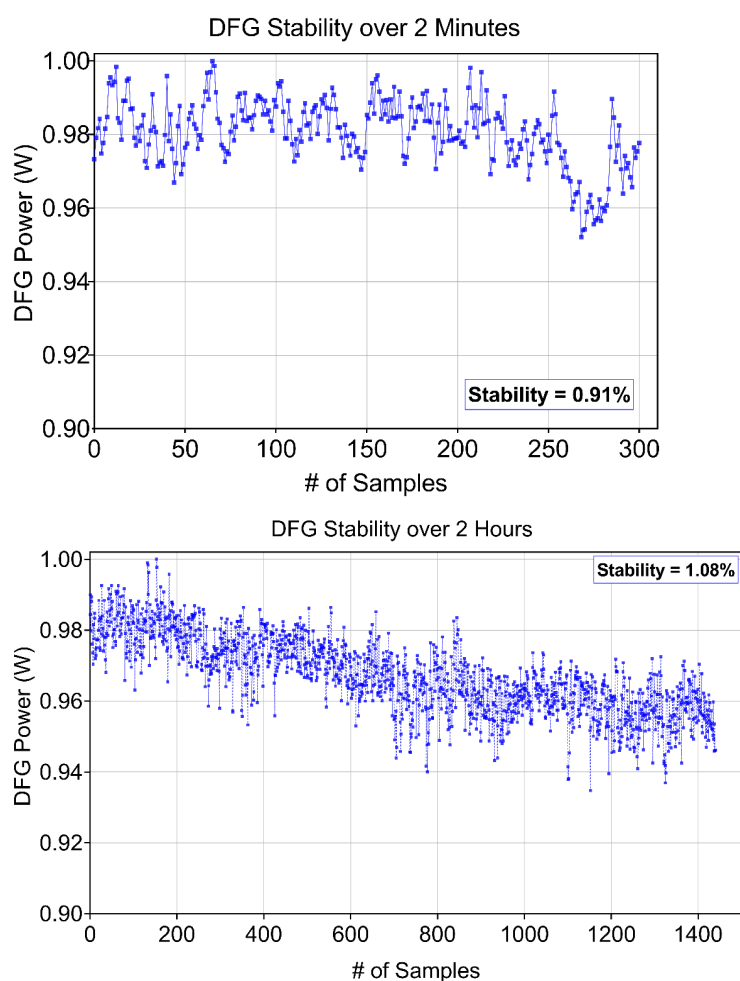


**Figure 7.** Measured DFG power fluctuations over short-term (2 min) and long-term (2 h) periods to assess stability. Power measurements were taken at intervals of 2 s for the short-term test and 5 s for the long-term test. The values are normalized to 1 for presentation purposes, and the actual DFG power corresponding to the figure is 63 mW, as stated in the manuscript.

High stability is essential for applications such as GHG detection, where consistent output power is crucial for accurate measurements.

Overall, our IC-DFG design achieves high efficiency and tunability while exhibiting robust stability, making it a promising candidate for real-world applications in environmental monitoring and satellite communication.

#### 4. Discussion

The results demonstrate promising performance with high efficiency, suggesting that our design is competitive with the state of the art. The achieved black-box efficiency is significantly higher than that of other systems, due, in part, to the direct-diode pumping approach used in this design. Notably, devices utilizing fiber amplification before pumping the nonlinear crystal have reported lower efficiencies, which we believe is because our approach avoids the additional losses associated with amplification stages. Additionally, the cavity enhancement factor of our system, driven by the high-quality optical coatings, is another contributor to the improved efficiency. For example, the Finesse of our cavity ( $\sim 200$ ) and the corresponding pump enhancement factor ( $\sim 30$ ) give it a distinct advantage over other systems like that of Witinski et al., who reported a Finesse of 65 and a pump enhancement factor of  $\sim 10$ .

Despite these successes, there are areas where improvements can be made. One area for potential improvement lies in the beam overlap. While the signal overlap with the current pump beam has been optimized, the 1064 nm pump itself is underfocused. Increasing the focus factor to  $\sim 2$  for the pump would lead to another similar jump in efficiency. However, implementing this improvement would likely require a redesign of the cavity and a re-evaluation of the focusing setup. Future experiments will need to explore the feasibility of decreasing the pump beam size or modifying the signal beam size to enhance overlap, although this may lead to some trade-offs in intensity.

Our theoretical analysis also indicates that there is room for further improvement. For example, increasing the pump power could potentially drive the circulating power even higher, improving the efficiency further. However, such changes would also bring new challenges, particularly with thermal lensing effects, which may compromise cavity stability as the pump and signal powers increase. Thermal effects, including those caused by multi-watt signal and pump powers, will need to be better understood and managed. While the current model approximates thermal lensing effects, a more comprehensive approach is necessary for future work.

In terms of device performance, we have identified areas where the design can be enhanced, such as improving the optical coatings and considering the nonlinear losses that become more pronounced with higher efficiency. These losses are currently not significant but could have a greater impact if the efficiency is pushed further. Nonlinear losses in the cavity, especially at higher powers, may also impact the overall performance, similar to previous observations in nonlinear processes like SHG. Future investigations will focus on understanding these effects more thoroughly.

Finally, in terms of application, the design shows great promise for portable mid-IR detectors. The compactness of our system, with a cavity length of less than 8 cm, along with the potential for a further reduction of this size, makes it suitable for remote sensing and gas detection. We have shown that it is possible to maintain high performance with shorter PPLN lengths, and ongoing efforts will aim to make the system even more portable. Moreover, we are exploring the use of this system in high-throughput secure networks, including the demonstration of mid-IR free-space optical links for atmospheric mitigation purposes.

## 5. Conclusions

In conclusion, our investigation demonstrates the successful development of a compact intracavity DFG mid-infrared laser with considerable potential for GHG detection and free-space optical communication applications. The optimization of the overlap efficiency has led to a black-box efficiency of  $3.4\% \text{ W}^{-1}$  and a maximum output power of 63 mW, achieved with a pump power of 4.7 W and a signal power of 380 mW. The design incorporates a PPLN crystal that enhances wavelength tunability, enabling a tuning bandwidth of about 50 nm in the mid-IR through various PPLN lengths. Furthermore, the stability of our system, assessed at 0.91% over 2 min and 1.08% over 2 h, confirms its reliability for precise measurements in applications such as greenhouse gas detection. Given these advancements, further gains in DFG output power should be possible through scaling the input signal power appropriately. The main limitation on output DFG power will likely be the increased thermal load on the PPLN as a result of this increased signal power. An interesting direction for future work would be detailed modeling of the thermal behavior of the PPLN at high power, perhaps through finite difference modeling. With these optimizations in mind, the current device is promising for enabling long-distance free-space links in the mid-infrared spectrum, fulfilling critical needs in environmental monitoring and advanced communication technologies.

## 6. Patents

This work is a developed version of the transmitter device laid out in the patent US20210141282A1—Mid-infrared wavelength optical transmitter and receiver.

**Author Contributions:** S.S.R.: Conceptualization, Investigation, Visualization, Writing—original draft, and Writing—review and editing. L.G.K.F.: Conceptualization, Methodology, Simulation, and Writing—review and editing. A.C.: Methodology, Visualization, and Writing—review and editing. T.K.: Methodology and Writing—review and editing, D.P.: Methodology, and Writing—review and editing. C.-Q.X.: Conceptualization, Methodology, and Writing—review and editing. All authors have read and agreed to the published version of the manuscript.

**Funding:** This research was funded by the Natural Sciences and Engineering Research Council of Canada (grant number RGPIN-2018-05501) and the High-Throughput and Secure Networks Challenge Program of the National Research Council of Canada (grant numbers HTSN-621 and HTSN-644).

**Institutional Review Board Statement:** Not applicable.

**Informed Consent Statement:** Not applicable.

**Data Availability Statement:** Data underlying the results presented in this paper may be obtained from the authors upon reasonable request.

**Acknowledgments:** The authors would like to thank Ali Atwi and Saeed Oghbaey from McMaster University for their valuable contributions. We also extend our gratitude to Saju Thomas of MDA (Kanata) and Atieh of Optiwave Systems Inc. for their helpful discussions.

**Conflicts of Interest:** The authors declare no conflicts of interest. The funders had no role in the design of the study; in the collection, analyses, or interpretation of the data; in the writing of the manuscript; or in the decision to publish the results.

## References

1. Khalighi, M.A.; Uysal, M. Survey on Free Space Optical Communication: A Communication Theory Perspective. *IEEE Commun. Surv. Tutor.* **2014**, *16*, 2231–2258. [[CrossRef](#)]
2. Kasyutich, V.L.; Holdsworth, R.J.; Martin, P.A. Mid-Infrared Laser Absorption Spectrometers Based upon All-Diode Laser Difference Frequency Generation and a Room Temperature Quantum Cascade Laser for the Detection of CO, N<sub>2</sub>O and NO. *Appl. Phys. B* **2008**, *92*, 271–279. [[CrossRef](#)]



3. Rehle, D.; Leleux, D.; Erdelyi, M.; Tittel, F.; Fraser, M.; Friedfeld, S. Ambient Formaldehyde Detection with a Laser Spectrometer Based on Difference-Frequency Generation in PPLN. *Appl. Phys. B* **2001**, *72*, 947–952. [[CrossRef](#)] [[PubMed](#)]
4. Richter, D.; Fried, A.; Weibring, P. Difference Frequency Generation Laser Based Spectrometers. *Laser Photonics Rev.* **2009**, *3*, 343–354. [[CrossRef](#)]
5. Hwang, A.Y.; Stokowski, H.S.; Park, T.; Jankowski, M.; McKenna, T.P.; Langrock, C.; Mishra, J.; Ansari, V.; Fejer, M.M.; Safavi-Naeini, A.H. Mid-Infrared Spectroscopy with a Broadly Tunable Thin-Film Lithium Niobate Optical Parametric Oscillator. *Optica* **2023**, *10*, 1535–1542. [[CrossRef](#)]
6. Flannigan, L.; Yoell, L.; Xu, C.Q. Mid-Wave and Long-Wave Infrared Transmitters and Detectors for Optical Satellite Communications—A Review. *J. Opt.* **2022**, *24*, 043002. [[CrossRef](#)]
7. Fischer, C.; Sigrist, M.W. Mid-IR Difference Frequency Generation. In *Solid-State Mid-Infrared Laser Sources*; Springer: Berlin/Heidelberg, Germany, 2003; pp. 99–143. ISBN 978-3-540-36491-7.
8. Myers, L.E.; Bosenberg, W.R.; Miller, G.D.; Eckardt, R.C.; Fejer, M.M.; Byer, R.L. Quasi-Phase-Matched 1064-Mm-Pumped Optical Parametric Oscillator in Bulk Periodically Poled LiNbO<sub>3</sub>. *Opt. Lett.* **1995**, *20*, 52–54. [[CrossRef](#)]
9. Xi, C.; Wang, P.; Li, X.; Liu, Z. Highly Efficient Continuous-Wave Mid-Infrared Generation Based on Intracavity Difference Frequency Mixing. *High Power Laser Sci. Eng.* **2019**, *7*, e67. [[CrossRef](#)]
10. Fejer, M.M.; Jundt, D.H.; Byer, R.L.; Magel, G.A. Quasi-Phase-Matched Second Harmonic Generation: Tuning and Tolerances. *IEEE J. Quantum Electron.* **1992**, *28*, 2631–2654. [[CrossRef](#)]
11. Myers, L.E.; Eckardt, R.C.; Fejer, M.M.; Byer, R.L.; Bosenberg, W.R. Progress in Quasi-Phase-Matched Optical Parametric Oscillators Using Periodically Poled LiNbO<sub>3</sub>. In *International Society for Optical Engineering*; SPIE: Bellingham, WA, USA, 1996; Volume 2700.
12. Cao, Z.; Han, L.; Liang, W.; Deng, L.; Wang, H.; Xu, C.; Zhang, W.; Gong, Z.; Gao, X. Ultrabroadband Tunable Continuous-Wave Difference-Frequency Generation in Periodically Poled Lithium Niobate Waveguides. *Opt. Lett.* **2007**, *32*, 1953–1955. [[CrossRef](#)]
13. Guha, S.; Falk, J. The Effects of Focusing in the Three-Frequency Parametric Upconverter. *J. Appl. Phys.* **1980**, *51*, 50–60. [[CrossRef](#)]
14. Flannigan, L.G.K.; Atwi, A.; Kashak, T.; Poitras, D.; Xu, C.Q. Compact Diode-Pumped Solid-State Laser with Intracavity Pump-Enhanced DFG Emitting at ~3.5 Microns. *Photonics* **2023**, *10*, 1164. [[CrossRef](#)]
15. Unger, S.; Schwuchow, A.; Jetschke, S.; Reichel, V.; Scheffel, A.; Kirchhof, J. Optical Properties of Yb-Doped Laser Fibers in Dependence on Codopants and Preparation Conditions. *Opt. Compon. Mater. V* **2008**, *6890*, 270–280.
16. Mishra, J.; McKenna, T.P.; Ng, E.; Stokowski, H.S.; Jankowski, M.; Langrock, C.; Heydari, D.; Mabuchi, H.; Safavi-Naeini, A.H.; Fejer, M.M. Mid-Infrared Nonlinear Optics in Thin-Film Lithium Niobate on Sapphire. *Optics* **2021**, *8*, 921–924.
17. Myslinski, P.; Nguyen, D.; Chrostowski, J. Effects of Concentration on the Performance of Erbium-Doped Fiber Amplifiers. *J. Light. Technol.* **1997**, *15*, 112–120. [[CrossRef](#)]
18. Guha, S.; Barnes, J.O.; Gonzalez, L.P. Multiwatt-Level Continuous-Wave Midwave Infrared Generation Using Difference Frequency Mixing in Periodically Poled Lithium Niobate. *Opt. Lett.* **2014**, *39*, 5018–5021. [[CrossRef](#)]
19. Huang, K.; Gan, J.; Zeng, J.; Hao, Q.; Yang, K.; Yan, M.; Zeng, H. Observation of Spectral Mode Splitting in a Pump-Enhanced Ring Cavity for Mid-Infrared Generation. *Opt. Express* **2019**, *27*, 11766–11775. [[CrossRef](#)]
20. Zhao, J.; Chen, Y.; Ouyang, D.; Liu, M.; Li, C.; Wu, X.; Xiong, X.; Mo, L.; Wang, M.; Liu, X.; et al. Over 3.8 W, 3.4 Mm Picosecond Mid-Infrared Parametric Conversion Based on a Simplified One-to-Many Scheme. *Opt. Express* **2024**, *32*, 8364–8378. [[CrossRef](#)]
21. Murray, R.T.; Runcorn, T.H.; Guha, S.; Taylor, J.R. High Average Power Parametric Wavelength Conversion at 331–348 Mm in MgO:PPLN. *Opt. Express* **2017**, *25*, 6421–6430. [[CrossRef](#)]
22. Ebrahim-Zadeh, M. New Frontiers in Optical Parametric Oscillators. In *Optics InfoBase Conference Papers*; Optica Publishing Group: Washington, DC, USA, 2018; Volume Part F123-LAOP 2018.
23. Zhang, G.J.; Gong, M.L.; Zhang, W.Q. Numerical Analysis of a Dual-Pass Pumping Laser with Weak Absorption. *Chin. Phys. B* **2017**, *26*, 50203. [[CrossRef](#)]
24. Risk, W.P. Modeling of Longitudinally Pumped Solid-State Lasers Exhibiting Reabsorption Losses. *J. Opt. Soc. Am. B* **1988**, *5*, 1412–1423. [[CrossRef](#)]
25. Boyd, R.W. *Nonlinear Optics*; Elsevier: Amsterdam, The Netherlands, 2020; ISBN 9780128110027.
26. Gayer, O.; Sacks, Z.; Galun, E.; Arie, A. Temperature and Wavelength Dependent Refractive Index Equations for MgO-Doped Congruent and Stoichiometric LiNbO<sub>3</sub>. *Appl. Phys. B* **2008**, *91*, 343–348. [[CrossRef](#)]
27. Chunosov, N.I. Rezonator. Available online: <http://rezonator.orion-project.org/> (accessed on 9 November 2024).
28. Kashak, T.; Flannigan, L.; Atwi, A.; Poitras, D.; Xu, C. Compact Intracavity Mid-Infrared Upconversion Detector—A Systematic Study. *Opt. Contin.* **2024**, *3*, 1660. [[CrossRef](#)]

29. Myers, L.E.; Eckardt, R.C.; Fejer, M.M.; Byer, R.L.; Bosenberg, W.R.; Pierce, J.W. Quasi-Phase-Matched Optical Parametric Oscillators in Bulk Periodically Poled LiNbO<sub>3</sub>. *J. Opt. Soc. Am. B* **1995**, *12*, 2102–2116. [[CrossRef](#)]
30. Dudzik, G.; Sotor, J.; Krzempek, K.; Sobon, G.; Abramski, K.M. Single-Frequency, Fully Integrated, Miniature DPSS Laser Based on Monolithic Resonator. In *Solid State Lasers XXIII: Technology and Devices*; SPIE: Bellingham, WA, USA, 2014; Volume 8959.

**Disclaimer/Publisher’s Note:** The statements, opinions and data contained in all publications are solely those of the individual author(s) and contributor(s) and not of MDPI and/or the editor(s). MDPI and/or the editor(s) disclaim responsibility for any injury to people or property resulting from any ideas, methods, instructions or products referred to in the content.